AGU PUBLICATIONS

JGR

Journal of Geophysical Research: Solid Earth

RESEARCH ARTICLE
10.1002/2017JB014746

Key Points:
- We study numerically the effects of fault roughness on the nucleation process during earthquake sequences
- Roughness complicates the nucleation process with asymmetric expansion of the rupture, multiple slip pulses, and larger nucleation length
- We derive an approximate solution for the nucleation length, which provides the roughness conditions under which faults can slip seismically

Correspondence to:
Y. Tal,
ytal@mit.edu

Citation:
Tal, Y., Hager, B. H., & Ampuero, J. P. (2018). The effects of fault roughness on the earthquake nucleation process. *Journal of Geophysical Research: Solid Earth*, *123*, 437–456. https://doi.org/10.1002/2017JB014746

Received 21 JUL 2017
Accepted 27 DEC 2017
Accepted article online 29 DEC 2017
Published online 15 JAN 2018

The Effects of Fault Roughness on the Earthquake Nucleation Process

Yuval Tal[1], Bradford H. Hager[1], and Jean Paul Ampuero[2]

[1]Earth Resources Laboratory, Department of Earth, Atmospheric and Planetary Sciences, Massachusetts Institute of Technology, Cambridge, MA, USA, [2]Seismological Laboratory, Division of Geological and Planetary Sciences, California Institute of Technology, Pasadena, CA, USA

Abstract We study numerically the effects of fault roughness on the nucleation process during earthquake sequences. The faults are governed by a rate and state friction law. The roughness introduces local barriers that complicate the nucleation process and result in asymmetric expansion of the rupture, nonmonotonic increase in the slip rates on the fault, and the generation of multiple slip pulses. These complexities are reflected as irregular fluctuations in the moment rate. There is a large difference between first slip events in the sequences and later events. In the first events, for roughness amplitude $b_r \leq 0.002$, there is a large increase in the nucleation length with increasing b_r. For larger values of b_r, slip is mostly aseismic. For the later events there is a trade-off between the effects of the finite fault length and the fault roughness. For $b_r \leq 0.002$, the finite length is a more dominant factor and the nucleation length barely changes with b_r. For larger values of b_r, the roughness plays a larger role and the nucleation length increases significantly with b_r. Using an energy balance approach, where the roughness is accounted for in the fault stiffness, we derive an approximate solution for the nucleation length on rough faults. The solution agrees well with the main trends observed in the simulations for the later events and provides an estimate of the frictional and roughness properties under which faults experience a transition between seismic and aseismic slip.

1. Introduction

A common view is that earthquakes occur via a shear rupture instability, in which the frictional resistance on a preexisting fault decreases with increasing sliding or sliding velocity (e.g., Scholz, 2002). As the instability occurs, the rupture propagates dynamically at a high speed close to the wave speed and with slip velocities much larger than the loading rate. Laboratory experiments on preexisting faults show that the development of the unstable rupture occurs via a nucleation process, which is characterized by roughly two phases: A quasi-static phase in which the rupture grows at a steady slow velocity with accelerating slip and a phase in which the rupture grows with accelerating speed (e.g., Dieterich, 1978; Kaneko et al., 2016; Latour et al., 2013; McLaskey & Kilgore, 2013; Nielsen et al., 2010; Ohnaka & Shen, 1999; Okubo & Dieterich, 1984).

Rate and state friction constitutive laws (Dieterich, 1979; Ruina, 1983) have emerged as powerful tools for investigating various earthquake phenomena, including earthquake nucleation (Marone, 1998). Numerical and theoretical models with rate and state fault friction are generally consistent with laboratory observations but provide additional insight into the nucleation process, as well as upscaling of the lab observations to natural faults. The models show that the exact behavior of the rupture during nucleation, and specifically how and to what extent the rupture expands between the initial localization of slip and slip rate and the dynamic stage of the rupture, is highly affected by the loading and initial conditions and the rate and state parameters and evolution laws (Ampuero & Rubin, 2008; Dieterich, 1992; Fang et al., 2010; Kaneko & Ampuero, 2011; Kaneko & Lapusta, 2008; Kato & Hirasawa, 1996; Lapusta & Rice, 2003; Noda et al., 2013; Rubin & Ampuero, 2005).

A source of complexity in the nucleation process is expected to arise from the deviation of faults from planarity. High-resolution map traces of large continental strike-slip earthquake surface ruptures and measurements of roughness on exhumed faults (Bistacchi et al., 2011; Brodsky et al., 2011; Brown & Scholz, 1985; Candela et al., 2009, 2012; Klinger, 2010; Power et al., 1987; Power & Tullis, 1991; Renard et al., 2006; Sagy et al., 2007) show that faults are rough at all scales and can generally be described as self-affine fractal surfaces. The roughness of faults can be measured by the average deviation of the profile from planarity

(RMS height), which for a profile with length L_f is expressed as $h(L_f) = b_r L_f^H$, where b_r is the RMS prefactor and H is the Hurst exponent. Candela et al. (2012) compiled roughness data over nine decades of length scales and suggested that natural faults have a self-affine roughness geometry with $H = 0.6$ and b_r ranging from 0.001 to 0.01 in the slip direction. However, while measurements at a particular wavelength bandwidth seems to fit $H = 0.6$, the data as a whole may be better fit with a larger value of H (Shi & Day, 2013).

Experimental observations show that, on the lab scale, roughness affects frictional constitutive parameters such as stress drop and critical slip-weakening distance and results in larger nucleation zones (Ohnaka, 2003; Ohnaka & Shen, 1999; Okubo & Dieterich, 1984). On the scale of natural faults, the effects of roughness are not yet clear. Numerical studies have focused, so far, on the static response of rough faults (e.g., Dieterich & Smith, 2009) or on the effects of roughness on the dynamic stage of the rupture (e.g., Bruhat et al., 2016; Dunham et al., 2011; Fang & Dunham, 2013; Shi & Day, 2013).

In this study, we use the numerical approach developed in Tal (2017) and Tal and Hager (2017) to explore the effects of roughness on the nucleation process of faults governed by rate and state friction laws. The simulations include sequences of at least two seismic cycles and thus enable us to examine the effect of the stress state and frictional conditions resulting from the rupture growth and arrest for a given slip event on the nucleation process at subsequent events. We focus on the scale of small earthquakes and consider faults with a length of 40 m. We choose the minimum roughness wavelength, $\lambda_{\min}$, to be at a size close to lab samples (20 cm) and thus use observed lab-scale rate and state friction laws without upscaling the constitutive parameters. In addition, we use the estimation of Fang and Dunham (2013) for the additional resistance to slip from fault roughness and balance the energy of an expanding rupture (e.g., Rubin & Ampuero, 2005) to derive an approximate solution for the nucleation length on rough faults governed by rate and state friction.

2. Model Description

We examine effects of roughness on the nucleation of shear rupture on a 40 m long finite fault embedded in a 2-D elastic medium with dimensions 120×80 m (Figure 1a). We assume a plane strain model and apply the following boundary and initial conditions: (1) a prescribed slow horizontal velocity of $V_b = \pm 10^{-9}$ m/s at the top and bottom boundaries of the medium; (2) zero vertical velocities on all the boundaries; (3) initial stresses σ_{xx0}, σ_{yy0}, and σ_{xy0}; and (4) horizontal normal tractions on the left and right boundaries, $\sigma_{bxx} = \sigma_{xx0}$. This setup enables completely spontaneous nucleation of the rupture. We do not explicitly consider pore fluids in this study and assume that the stresses are effective stresses if the medium is saturated with fluids. We perform 25 simulations. We consider three different fault geometries of self-affine fractals with Hurst exponent of $H = 0.8$, Geo-1, Geo-2, and Geo-3 (Figure 1b). For each geometry, we generate eight profiles, in which b_r ranges between 0.001, 0.002, 0.005, and 0.01 and $\lambda_{\min}$ ranges between 0.2 m and 1 m. For reference, we also run a simulation with a smooth fault.

The fault is governed by rate and state friction, which is given in the standard aging formulation (Dieterich, 1979; Ruina, 1983) by

$$\mu = \mu^* + a\ln\left(\frac{v + v_{th}}{v^*}\right) + b\ln\left(\frac{L\theta}{v^*}\right) \tag{1}$$

$$\dot{\theta} = 1 - \frac{\theta(v + v_{th})}{L}, \tag{2}$$

where a and b are rate and state constitutive parameters, v is the slip rate, v^* is a reference slip rate, μ^* the steady state friction at $v = v^*$, θ is a state variable, and L is the characteristic sliding distance. We add a threshold velocity term, $v_{th}=10^{-13}$ m/s, to avoid singularity at $v = 0$. We do not consider the effect of normal stress variations on θ. The mechanical properties of the medium, friction law parameters, and initial stresses are given in Table 1. We use here the aging law for the state evolution law, which incorporates healing of the fault in stationary contact. We note that recent studies suggest that the "slip" evolution law provides a better fit to velocity-jump rock friction experiments (e.g., Bhattacharya et al., 2015, 2017; Rathbun & Marone, 2013). Ampuero and Rubin (2008) showed that these two slip laws result in differences in the nucleation process on smooth faults; it would be important to examine the behavior of rough faults governed by rate and state friction with the slip evolution law in future studies.

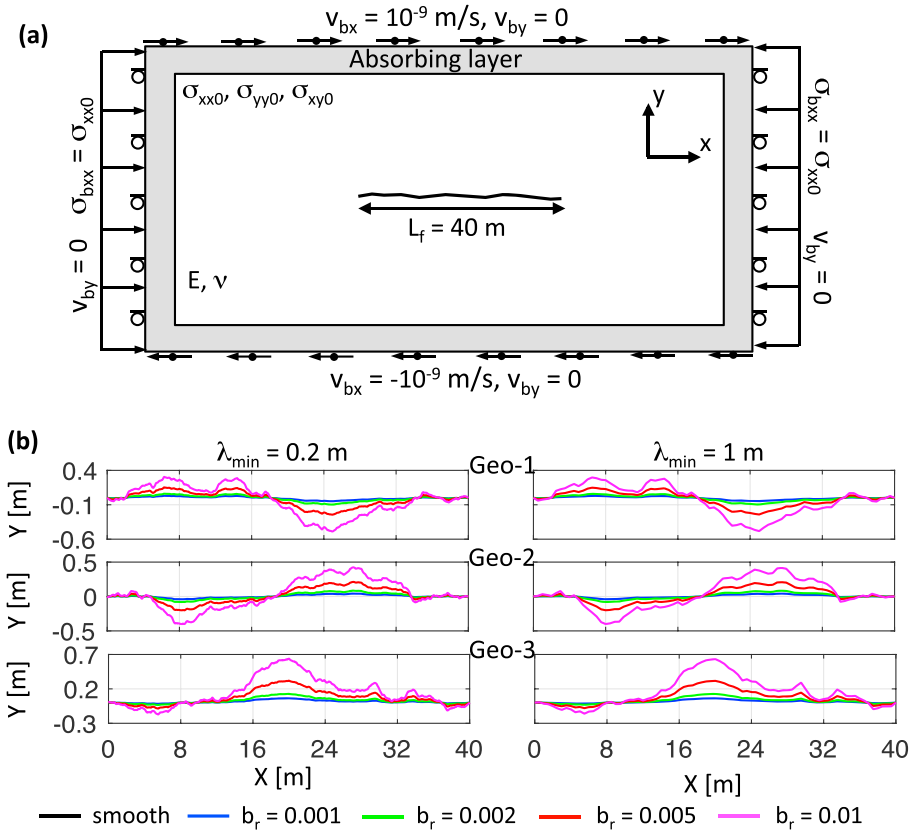

Figure 1. (a) The problem setup: a 40 m long finite fault is embedded in a 2-D elastic medium with dimensions 120 × 80 m, which is subjected a prescribed slow horizontal velocity $V_b = \pm 10^{-9}$ at the top and bottom, zero vertical velocities on all the boundaries, initial stresses σ_{xx0}, σ_{yy0}, and σ_{xy0}, and horizontal normal tractions on the left and right boundaries $\sigma_{bxx} = \sigma_{xx0}$. During the dynamic stages, the model includes an absorbing layer with gradual Rayleigh damping. (b) The fault profiles examined in this study. We consider three different general geometries, and for each geometry, eight profiles are generated with roughness prefactor values of b_r = 0.001, 0.002, 0.005, and 0.01 and minimum wavelength of λ_{min} = 0.2 m and 1 m. For reference, we also run a simulation with a smooth fault.

Table 1
Model Parameter Values

Parameter		Value
Frictional properties		
Direct-effect parameter	a	0.01
Evolution-effect parameter	b	0.012
Reference velocity	v^*	10^{-6} m/s
Reference friction	μ^*	0.6
Characteristic sliding distance	L	20 μm
Initial friction	μ_0	0.57
Initial state variable	θ_0	1 s
Bulk properties		
Young's modulus	E	60 GPa
Poisson's ratio	ν	0.25
Density	ρ	2,700 kg/m^3
Initial remote stresses		
Horizontal stress	σ_{xx0}	100 MPa
Vertical stress	σ_{yy0}	100 MPa
Shear stress	σ_{xy0}	57 MPa

Our numerical approach (Tal, 2017; Tal & Hager, 2017) is based on the mortar finite element formulation (Bernardi et al., 1993), in which nonmatching meshes are allowed across the fault and the contacts are continuously updated; thus, it enables slip that is large relative to the size of the elements near the fault, as well as an accurate modeling of the variation of normal stress during slip. We extend the 2-D large sliding mortar formulation of Popp et al. (2009) and Gitterle et al. (2010) to dynamic problems and consistently implement the rate and state friction law into the method. The method uses Lagrange multipliers with dual spaces discretization (Wohlmuth, 2000) to enforce the continuity of stress, nonpenetration condition, and frictional resistance on the fault in a weak integral sense. This concept is combined with the primal-dual active set strategy (Brunssen et al., 2007; Hüeber et al., 2008; Hüeber & Wohlmuth, 2005) to enable an efficient local elimination of the discrete Lagrange multipliers by static condensation and an efficient semi-smooth Newton algorithm for the solution of the nonlinear system of equations. Moreover, the discretization of the friction law involves a procedure to condense out the state variables, thus eliminating the addition of another set of unknowns into the system. The method

uses a quasi-static backward Euler time discretization scheme when inertial effects are negligible and implicit Newmark scheme (Newmark, 1959) for dynamic analysis. Because both schemes are implicit, the implementation of variable time stepping is straightforward, and the whole seismic cycle can be modeled, including a completely spontaneous nucleation process.

We use a variable time step size: Based on the current values of slip rates, we estimate the time step size at the next time step such that the average incremental slip of the 40 fastest nodes along the fault is generally below 0.4 L (Appendix A). This procedure results in a time step size that represents the evolution of the friction coefficient well without reducing the time step size to values that lead to simulations with an excessive number of time steps. We switch between quasi-static and dynamic time integration schemes when the average slip rate at the 40 fastest nodes on the fault is larger than 5×10^{-5} m/s. For the dynamic stages, we use the Newmark time integration scheme with small algorithmic damping ($\beta = 0.35$ and $\gamma = 0.7$) and also add an absorbing layer with gradual Raleigh damping near the boundaries of the model. We refine the mesh around the fault with hanging nodes in order to represent the geometry of the fault properly. This results in 2,561 nodes along the fault with a mesh spacing of 1.56 cm, which is equal to $\lambda_{min}/13$ and $\lambda_{min}/64$ for $\lambda_{min} = 0.2$ m and 1 m, respectively. Under plane strain conditions, the smallest length scale to be resolved numerically for a growing nucleation zone on a fault governed by rate and state friction with the aging law scales roughly as $L_b = \frac{G}{1-\nu}\frac{L}{b\sigma}$ (Ampuero & Rubin, 2008). Here σ is the normal stress and G and ν are the shear modulus and Poisson's ratio of the medium, respectively. With the parameters adopted in this study (Table 1), the average $L_b \approx 53.3$ cm and is resolved with about 34 elements.

Currently, the numerical method accounts only for an elastic rheology of the medium surrounding the fault. This approximation limits the amount of deformation that the medium can experience before unrealistic stresses larger than the Coulomb failure criterion accumulate in the material around the fault. Therefore, we set the total time of the simulation to the time during which two large events would occur, if a smooth fault were considered. Because we do not model a long sequence of earthquakes, the initial conditions have a significant effect on the results, despite the spontaneous nucleation. We conceptually begin the simulation at the end of an earthquake that ruptured the whole fault and choose the initial friction parameters accordingly. We assume that the earthquake approached a slip rate on the order of 1 m/s during the rupture and that the state variable and the friction coefficient had no time to evolve and are equal to their steady state values at this slip rate, $\theta_0 = L/1$ and $\mu_0 = \mu^* + (a - b)\ln(1/v^*) \approx 0.57$, respectively. The initial shear stress is chosen such that $\sigma_{xy0} = \mu_0\sigma_{yy0}$. As the roughness of the fault increases, some segments along the fault may begin to slip under smaller shear stress. In these cases, the initial shear stress is smaller than $\mu_0\sigma_{yy0}$, but in order to maintain similar initial conditions in all simulations, we do not allow the state variable to evolve until the remote shear stress exceeds σ_{xy0}.

3. Results

3.1. The Nucleation Process

To study the nucleation process, we need to define when the nucleation process begins, and when nucleation ends and the dynamic stage begins. For the friction parameters adopted in this study, the nucleation process involves stages both of localization and expansion of the rupture with accelerating slip rates (Rubin & Ampuero, 2005). The determination of the exact stage in which those processes start is somewhat subjective and becomes more complex with the addition of roughness. Therefore, we determine the beginning of the nucleation stage, from peaks in curves of the time evolution of the average shear traction on the fault, τ_{av} (Figure 2a). With this choice, the nucleation process may begin after the beginning of the localization, but this has no effect on the findings described in this paper.

The transition to the dynamic stage of the rupture is defined at the time at which both the moment rate per unit length, $\dot{M}_{0,1d} = G\int_{L_f} v(x,t)\mathrm{d}x$, is larger than a threshold value of 5×10^9 N/s and an active slip pulse moves at a speed larger than a threshold of 20% of the shear wave speed of the surrounding medium. Because with increasing roughness there are many fluctuations in the rupture velocity v_r, the latter threshold is larger than that used by Kaneko and Lapusta (2008). Figure 2b shows the evolution of τ_{av} during the first slip events in the sequences obtained for faults with $\lambda_{min} = 0.2$ m, and $b_r = 0.001$ and 0.002, as well as the transition to the dynamic stage. The nucleation begins with a very small decrease in τ_{av}, over a time of

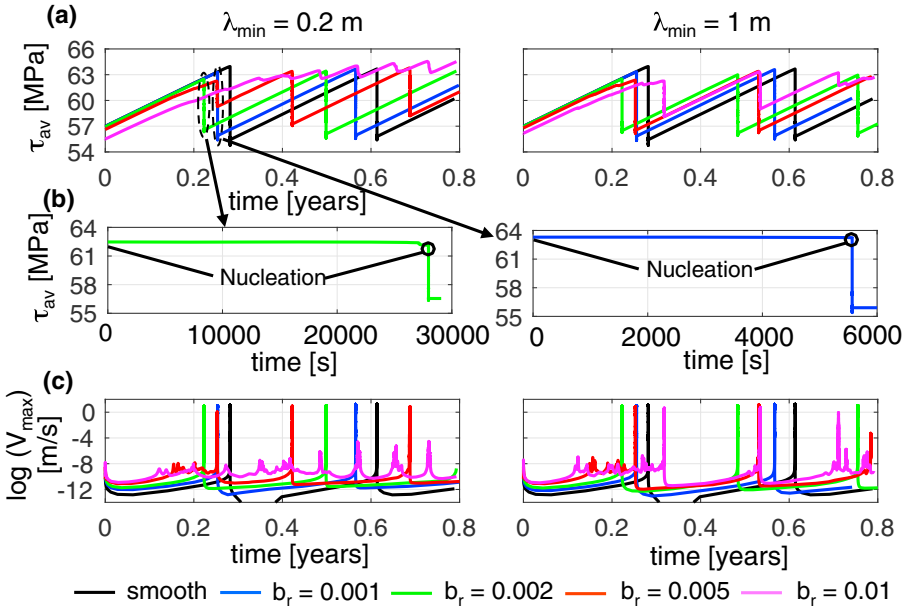

Figure 2. (a) The evolution of τ_{av} versus time for the eight profiles of Geo-1, as well as for a smooth fault. (b) The evolution of τ_{av} versus time during the first slip events in the sequences obtained for faults with λ_{min} = 0.2 m, and b_r = 0.001 (right) and 0.002 (left). (c) The evolution of the maximum slip rate on the fault versus time for the eight profiles of Geo-1, as well as for smooth faults.

about 5,500 s and 27,000 s for b_r = 0.001 and 0.002, respectively. For b_r = 0.002, the nucleation includes another stage of moderate decrease in τ_{av} over about 1,000 s, in which there are some fluctuations in the rate of decrease. After the transition to the dynamic stage of the rupture, there is a rapid decrease in τ_{av}. For b_r = 0.001, there is a sharper transition into the dynamic stage.

To examine the effect of roughness on the nucleation process, Figure 3 shows the evolution of slip u, slip rate v, and the friction coefficient μ along the fault during the sequences obtained for a smooth (planar) fault and for a rough fault with Geo-1, b_r = 0.001, and λ_{min} = 0.2 m. The evolution of μ is shown only for the first slip event in each sequence. We show here the evolution of μ, rather than the shear stress, because the large spatial variations in the normal and shear tractions on rough faults mask the behavior of the rupture. The contours of u are plotted for the loading, nucleation, and dynamic (propagation and arrest) stages of the seismic cycle. In the case of the first event of the sequence obtained for a smooth fault, the contours of v and μ are plotted for the nucleation and the whole dynamic stage. However, for better visualization of the nucleation stage, the contours of v and μ are shown only for the nucleation stage and for the beginning of the dynamic stage in other slip events.

We begin with examining the behavior of the smooth fault (Figures 3a, 3c, and 3e). Because the fault is finite, at the beginning of the first slip event on the smooth fault, the profiles of u and v have a maximum value at the center of the fault. Correspondingly, μ shows a very small reduction of about 0.02% at the center. Consequently, there is a localization of u and v and further decrease in μ at the center, which is followed by expansion of the rupture in a crack-like fashion, with peaks in v and μ near the tips and relatively uniform values in the interior. This behavior was also observed in the simulations of Rubin and Ampuero (2005) and Fang et al. (2010) when similar a/b values where used. Both v and v_r increase as the rupture expands, and the nucleation length l_{nuc}, defined as the total length of the rupture at the transition to the dynamic stage, is about 5.6 m. Note that we use the total length of the rupture, while some studies refer to the half rupture length. The complex arrest of the rupture and the dynamic effects result in nonuniform distributions of μ and v at the end of the slip event, with maximum values about 5 m from the ends of the fault. These become the initial condition for the second slip event, which begins with a localization of u and v at two locations 5.5 m from the left and right ends of the fault. However, because of small numerical errors during the dynamic stage of the rupture, the profiles of u and v are not perfectly symmetric; they have slightly larger

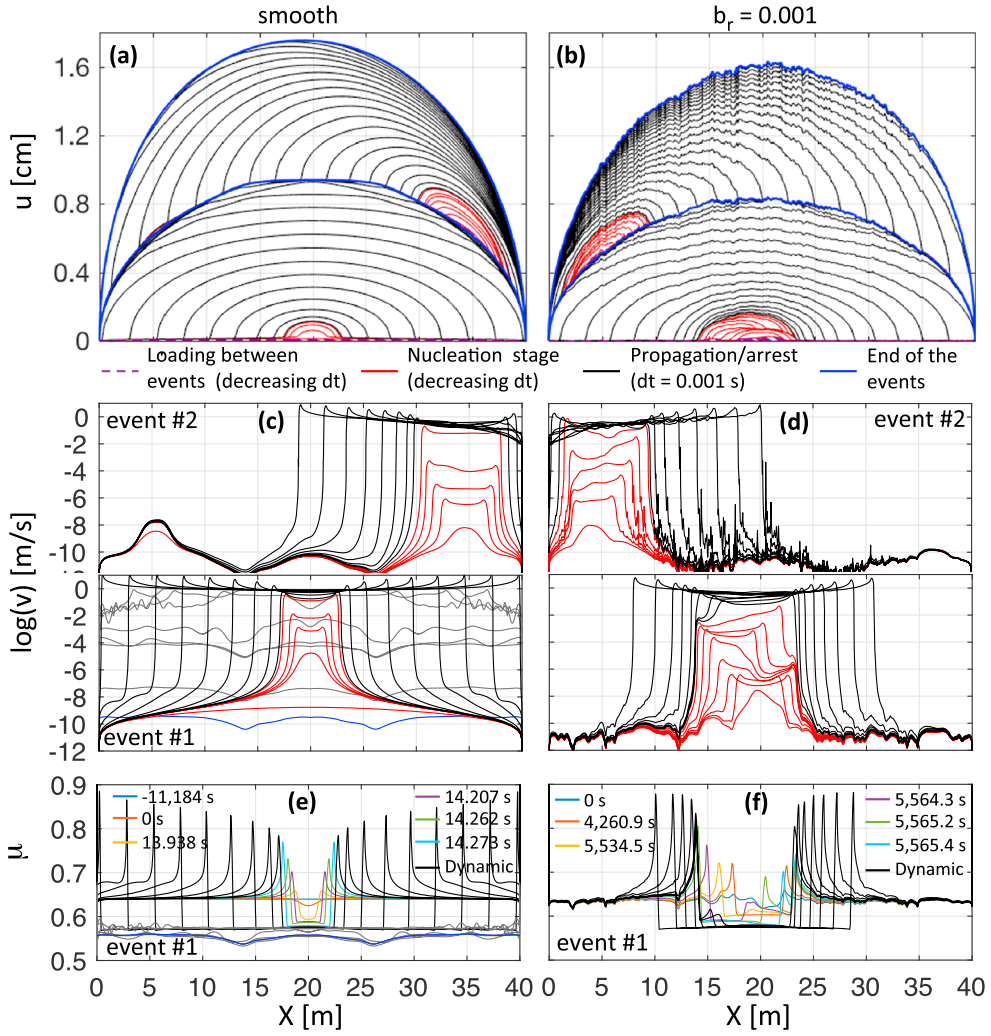

Figure 3. Profiles of u, v, and μ along the fault for a (a, c, and e) smooth fault and a (b, d, and f) rough fault with Geo-1, $b_r = 0.001$, and $\lambda_{min} = 0.2$ m. The time interval between the contours is variable for the loading and nucleation stages and equal to 1 ms for the dynamic stage. The contours of μ are shown only for the first slip event in each sequence. The contours of u are plotted for all the stages in the seismic cycle, that is, the loading (dashed purple), nucleation (red), and dynamic (black) stages, where the dynamic stage includes both the propagation and arrest of the rupture. The final stage of each slip event is shown in blue. In the case of the first event of the sequence obtained for a smooth fault, the contours of v and μ are plotted for the whole dynamic stage, with gray contours for the arrest phase. However, for better visualization of the nucleation stage, the contours of v and μ are shown only for the nucleation stage and the beginning of the dynamic stage in other slip events. Moreover, the contours of μ are shown only for the first event in each sequence and we plot only six contours (with different colors) for the nucleation stage.

values at the right-hand side. This leads to rupture nucleation on the right side of the fault, again in a crack-like fashion, but with some effects of the location being close to the end of the fault. The nucleation length is larger, with $l_{nuc} \approx 8.5$ m. It is important to note that, practically, the effect of numerical errors, which leads to the break in the symmetry of the second slip event, is negligible because it is much smaller than the effect of any heterogeneity of the fault.

In the case of a rough fault with Geo-1, $b_r = 0.001$, and $\lambda_{min} = 0.2$ m (Figures 3b, 3d, and 3f), the nucleation process is more complex and highly affected by local geometric barriers, which slow down the expansion of the rupture and the increase in slip rate. At the beginning of the first slip event, there are already localizations of u and v, with the maximum values on a 5 m long segment at the center of the fault. A portion of this segment also experiences a reduction of about 2% in μ. It is important to note that the rupture initiates in this

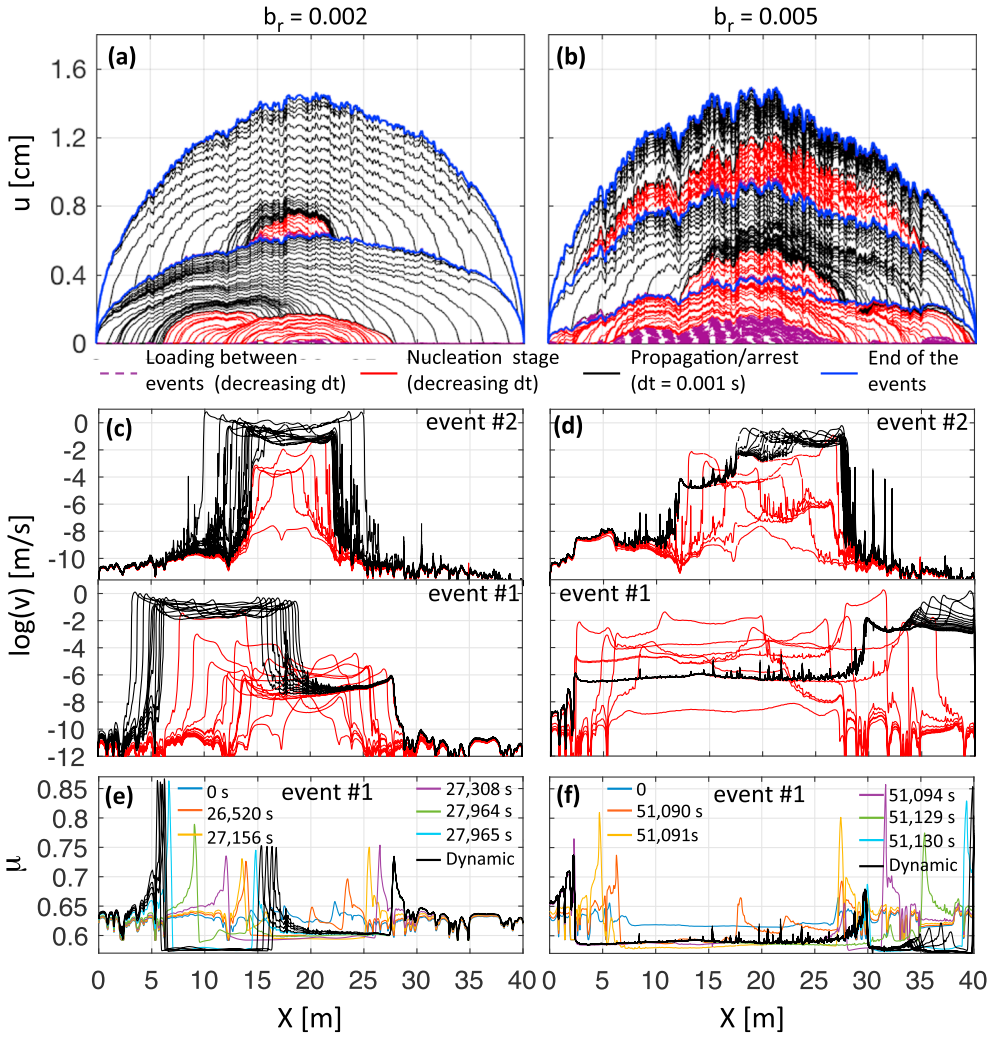

Figure 4. Profiles of u, v, and μ along rough faults with Geo-1, $\lambda_{min} = 0.2$ m, and (a, c, and e) $b_r = 0.002$ and (b, d, and f) 0.005. The contours of u are plotted for all the stages in the seismic cycle, that is, the loading (dashed purple), nucleation (red), and dynamic (black) stages, where the dynamic stage includes both the propagation and arrest of the rupture. The time interval between the contours is variable for the loading and nucleation stags and equal to 1 ms for the dynamic stages. The final stage of each of the slip events is shown in blue. For $b_r = 0.005$, the contours of v are shown only for the first and second slip events of the sequence. For better visualization of the nucleation stage, the contours of v and μ are shown only for the nucleation stage and the beginning of the dynamic stage. Moreover, the contours of μ are shown only for the first event in each sequence and we plot only six contours (with different colors) for the nucleation stage.

location because of the local slope of the fault (see Figure 1), rather than the effect of the finiteness of the fault. The slip rates at the beginning of the expansion process are a few orders of magnitude smaller than those in the initial event on the smooth fault. In general, smaller slip rates at this stage promote more expansion of the rupture before the transition to the dynamic stage (Fang et al., 2010). The rupture expands to both sides and develops peaks in v and μ near the tips, but then it approaches a barrier on the right and expands much faster to the left as a unilateral pulse. When the slip rate on the left front is about 10^{-3} m/s, a new slip pulse initiates on the left and propagates to right on the existing rupture. Because of a barrier on the left front of the rupture, the new pulse becomes more dominant and has a larger v. At the transition to the dynamic stage of the rupture, the total length of the rupture is about 9 m and there is a new pulse that propagates to the left. As new pulses initiate later in the nucleation process, the rerupturing process is associated with a smaller peak in μ, as well as a smaller reduction. As they join the stationary pulses at the fronts of the rupture, the peaks in μ instantaneously increase. Similar to the

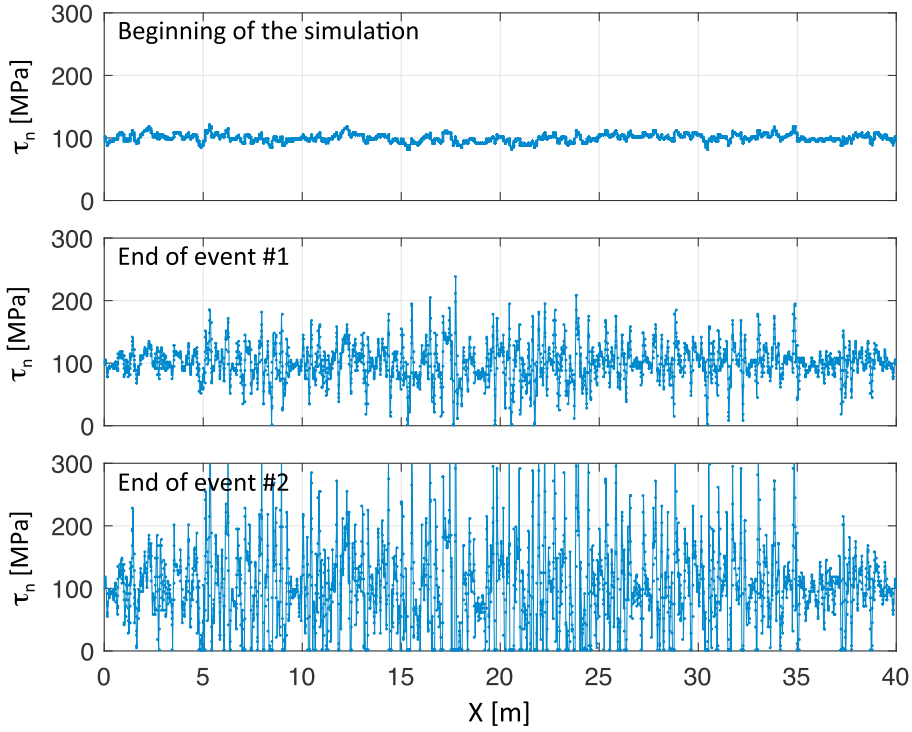

Figure 5. The normal tractions along the fault at the beginning of the simulation and at the ends of the first and second slip events for fault with Geo-1, $b_r = 0.005$, and $\lambda_{min} = 0.2$ m. Note that at the end of the second slip event, the normal traction is slightly larger than 300 MPa for some of the nodes.

behavior observed on the smooth fault, the second slip event also starts next to one of the ends of the rough fault. The nucleation process during the second event is somewhat less complex than that of the first. Note that for the second slip event, the slip rates at the beginning of the expansion process are similar to those in the second slip event on the smooth fault, and consequently, they both have similar nucleation lengths.

In general, the complexity of the nucleation process increases as b_r increases. In the first slip event on the fault with Geo-1, $b_r = 0.002$, and $\lambda_{min} = 0.2$ m (Figures 4a, 4c, and 4e), the nucleation stage involves many new slip pulses, as well as stages where v decreases as the rupture grows. Moreover, the complexity in the nucleation process and the lower slip rates in the beginning of the expansion process lead to a large nucleation length of $l_{nuc} \approx 22$ m. Similar to the fault with $b_r = 0.001$, the second slip event shows simpler behavior and larger slip rates at the beginning of the expansion process; thus, the nucleation length is small. In the case of the rough fault with Geo-1, $b_r = 0.005$, and $\lambda_{min} = 0.2$ m (Figures 4b, 4d, and 4f), there are three slip events. The first slip event is almost completely aseismic, with only 3% of the total slip occurring during the dynamic stage of the rupture. Moreover, the loading stage involves much slip, which is partly accumulated during very slow slip events with a maximum slip rate of $v \sim 10^{-8}$ m/s (see Figure 2c). Because these events barely affect the evolution of the average shear stress on the fault, they are not considered here as separate slip events. The nucleation lengths of the second and third slip events are $l_{nuc} \approx 15$ and 33 m, respectively, and about 40% of the slip accumulated during the third slip event is aseismic.

As b_r increases, for slip events later in the sequences, small regions along the fault begin to open and the number of nodes that are not in contact increases. For example, Figure 5 shows the normal tractions at the beginning of the simulation and at the end of the first and second slip events on the fault with Geo-1, $b_r = 0.005$, and $\lambda_{min} = 0.2$ m. The spatial variations in the normal tractions generally correspond to the minimum wavelength; there are 14 noncontact nodes at the end of the first slip event and 280 at the end of the second slip event. When the active rupture passes through these nodes, they slip at rates similar to their neighboring nodes. However, noncontact nodes that are not on the active rupture, because of the dynamic waves radiated by the rupture, experience substantial variation in v, including transitions to negative values,

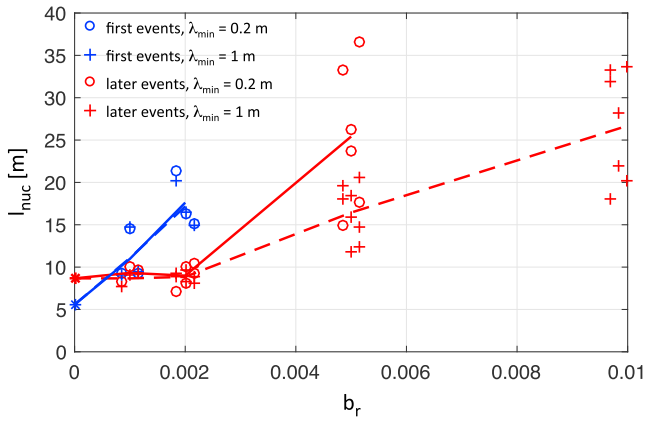

Figure 6. The nucleation lengths of the fast slip events in the 25 simulated earthquake sequences. Only slip events where the slip accumulated during the dynamic stage of the rupture is more than half of the total slip are considered. Slip events that are the first in the sequence are shown in blue, while later events are shown in red, both with open circles for faults with λ_{min} = 0.2 m and "plus" symbols for faults with λ_{min} = 1 m. The curves represent the average values for the first (blue) and later (red) slip events on faults with λ_{min} = 0.2 m (solid) and λ_{min} = 1 m (dashed).

where the logarithm is undefined. Moreover, the value of μ for the non-contact nodes is meaningless. Therefore, we do not plot the values of μ and v at the stages when they are not in contact.

At stages when a portion of the fault already slips at a large slip rate, there are spikes, with large values of v at regions on the fault that are not part of the active rupture. These spikes correspond to nodes where the normal traction continuously decreases. As the normal traction decreases, there is a positive feedback: the decrease in the resistive forces leads to an increase in v and u, which leads to a further decrease in the normal traction. The slip rate at the spikes is significantly larger than for the surrounding nodes but is generally smaller than 10^{-4} m/s. At these slip rates, the strain is so small that the deformation can be very local. Note also that the fault includes 2,561 nodes; thus, spikes that include several nodes also appear highly localized in the plots.

3.2. Nucleation Length

The nucleation lengths, l_{nuc}, of the fast slip events in the 25 simulated earthquake sequences are summarized in Figure 6. Only slip events where the slip accumulated during the dynamic stage of the rupture is more than half of the total slip are considered. In general, l_{nuc} increases with increasing slope as b_r increases, but there is also substantial variability in the values as b_r increases. A significant effect is observed for whether the slip event is first or later in the sequence, where except for the smooth fault, the values of l_{nuc} in the first slip events are larger than those of later events. In the case of the first slip events, l_{nuc} increases rapidly with b_r for $b_r \leq 0.002$ and there are no fast slip events for larger b_r values. For slip events later in the sequence, there is a very small increase in l_{nuc} with b_r for $b_r \leq 0.002$ and a large increase for higher b_r values. The effect of λ_{min} on l_{nuc} is negligible for $b_r \leq 0.002$. As b_r increases, l_{nuc} significantly increases with decreasing λ_{min}, where for $b_r = 0.01$, there are fast slip events only for $\lambda_{min} = 1$.

The nucleation lengths obtained here for smooth faults are generally consistent with those in the studies of Rubin and Ampuero (2005) and Fang et al. (2010). Rubin and Ampuero (2005) used a fracture energy balance to show that in the limit of large slip rates the nucleation length on smooth faults asymptotically approaches

$$l_c = \frac{2G^* Lb}{\pi\sigma(b-a)^2}, \tag{3}$$

where for plane strain $G^* = G/(1-\nu)$. How closely the nucleation length approaches l_c depends on the loading rate and the initial conditions, which significantly affect the nucleation-zone expansion process (e.g., Fang et al., 2010; Rubin & Ampuero, 2005). In this study, the values of l_{nuc} for the first and second slip events on the smooth fault are $0.45l_c$ and $0.7l_c$, respectively.

3.3. Initiation of the Rupture

3.3.1. Location on the Fault

In all slip events, the nucleation process begins with localization of slip and slip rate and local reduction in the frictional resistance (see Figures 3 and 4). In this section, we examine the effects of roughness on the location where the nucleation process of fast slip events initiates, as well as the effects of the final conditions of the preceding slip events when the slip events are later in the sequence. As mentioned earlier, we define the beginning of the slip events at peaks in curves of the time evolution of the average shear stress on the fault. However, as the roughness increases, more slip is accumulated during the loading stage and the localization process begins in multiple regions before the beginning of the slip event (as we defined it), although with very small slip rates. We are interested in the region in which the actual rupture initiates, and we study the location of this region in the rest of this section. To define an exact location, we search for a peak in the slip accumulated during the loading stage in this region (Figure 7). It is important to note that the complex nucleation process on rough faults may lead to a completely different location of the final slip pulse at the transition to the dynamic stage.

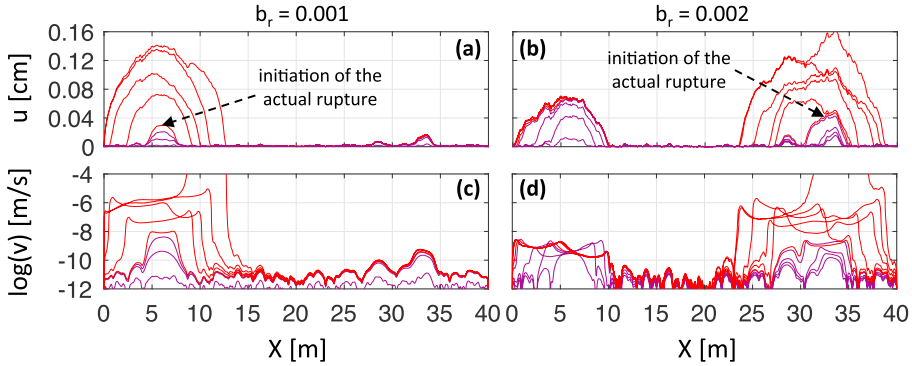

Figure 7. Profiles of u and v for the loading (purple) and the beginning of the nucleation stage (red) during the first slip events in the sequences obtained for faults with Geo-2, λ_{min} = 0.2 m, and (a and c) b_r = 0.001 and (b and d) 0.002.

In the first fast slip events in the earthquake sequences, the ruptures initiate at the center of the fault for Geo-1, 6–8 m from the ends of the fault for Geo-2, and 2.5 m from the center of the fault for Geo-3 (Figure 8). These locations correspond to regions on the faults where the orientation is preferable for slip, that is, regions with relatively large negative slopes of the fault topography and with no adjacent geometric barriers with a large positive slope. Note that the figure shows the absolute distance of the initial localization from the center of the fault $|x_{ini}|$. In the case of Geo-2 and λ_{min} = 0.2 m, the initiation of the actual rupture occurs at the left side of the fault for b_r = 0.001 (Figure 7). For b_r = 0.002, the slope of this section is more negative; thus, it starts to slide under smaller loading and the available energy is smaller. Moreover, the rupture has to propagate through barriers with larger amplitude. Therefore, the slip rate on this section does not accelerate and the actual rupture initiates on a section on the right that accumulated less slip during the loading stage.

For slip events that are later in the sequences, $|x_{ini}|$ is determined by both the state of stress at the end of earlier events and the geometry of the fault. For $b_r \leq 0.001$, the later events initiate 4–6 m from the ends of the fault, where the shear stress at the end of preceding slip events is maximal. As b_r increases, the effect of the geometry becomes more important. In the case of faults with $b_r \geq 0.005$ and Geo-1, the location where the later events initiate is always next to the center, but for Geo-2 and Geo-3 it is more scattered between few regions where the geometry of the fault is more favorable for slip.

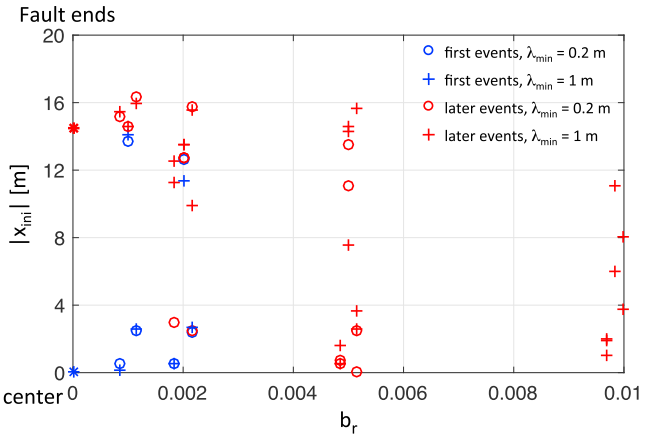

Figure 8. The locations where the fast slip events in the 25 simulated earthquake sequences initiate at the beginning of the nucleation stage. The plot shows the absolute distance of the locations from the center of the fault. Slip events that are the first in the sequence are shown in blue, while later events are shown in red, both with open circles for faults with λ_{min} = 0.2 m and plus symbols for faults with λ_{min} = 1 m.

3.3.2. Loading Stage

To examine further the initiation of the rupture in later events, Figure 9 shows the evolution of shear tractions τ_t, v, θ, and μ at six loading stages between the end of the first slip event and the beginning of the second slip event for a smooth fault and a fault with Geo-1, b_r = 0.002 and λ_{min} = 1 m. The figure also shows the six loading stages on curves of the average shear stress on the fault versus time. For both geometries, the distributions of v, θ, and μ at stage #1 are not correlated with the local geometry of the fault. They result from the finiteness of the fault and the complex arrest of the rupture during the first slip event. The maximum values of v and μ at this stage are at both X = 5 and 35 m for the smooth fault and X = 5 m for the rough fault. For the rough fault, there are large spatial variations in τ_t, which correlate with $\lambda_{min}/2$. These are due to changes in the normal tractions on the fault as it slipped during the first slip event. Note that stage #1 is defined at the stage where the average stress begins to increase consistently with time, which is 500–800 s after the dynamic stage of the rupture (see Figure 9).

Consider the smooth fault. At stage #2, all the nodes on the smooth fault are in a stuck state; thus, the slip rate considered for the friction calculation is the threshold velocity (equations (1) and (2)) and μ is spatially constant. However, this does not seem to be an important issue

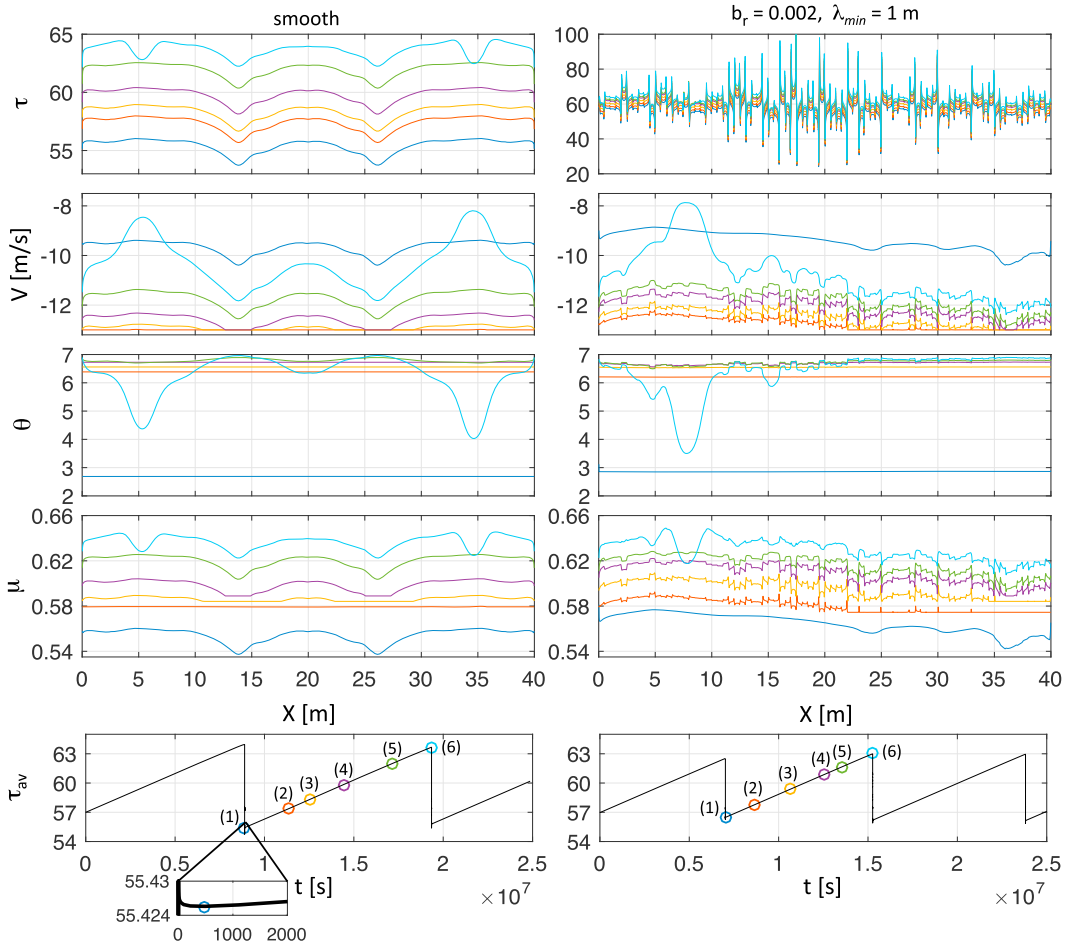

Figure 9. The evolution of shear tractions τ_t, v, θ, and μ at six loading stages between the end of the first slip event and the beginning of the second slip event for a smooth fault and a fault with Geo-1, b_r = 0.002 and λ_{min} = 1 m. The six loading stages are shown on the curves of the average shear stress on the fault versus time.

because the shear tractions are not affected by the threshold velocity. At stages 3–5, τ_t, v, and μ increase with time, maintaining their distribution from stage 1. At stages 1–4, the term $v\theta$/L in equation (2) is much smaller than one; thus, θ is spatially constant and equal to the time from the dynamic stage of the first slip event. At stage #5, θ varies spatially with a distribution that is a mirror image of the distributions of τ_t, v, and μ. At stage #6, the localization in v begins, with a maximum value at $X \approx 34.5$ m. Correspondingly, there are reductions in τ_t, θ, and μ in this region.

For the rough fault, some of nodes are at a stuck state with constant value of μ at stage #2, while other nodes slip with different values of v and μ. The large-scale distributions of v and μ at the slipping nodes correspond to their distributions at the end of the first slip event, but there are also small-scale variations that correspond to the roughness and the spatial variations of the normal tractions. At stages 3–5, τ_t, v, and μ increase with time, but the amplitude of the small-scale variations in v and μ decreases, especially on the left side of the fault, where both are larger. At stages 1–3, θ is spatially constant and equal to the time from the dynamic stage of the first slip event, while at stages 4–5 it varies spatially with a distribution that is a mirror image of the distributions of v and μ. At stage #6, v does not localize exactly at the region where the values of v and μ are maximum at stage #1, but there is a shift of 2.5 m to the right because the localization cannot take place on a region where the slope of the fault is positive, especially as b_r increases. The small-scale variations in v that correspond to $\lambda_{min}/2$ are not observed in the region where the localization occurs. The localization is accompanied by reductions in τ_t, θ, and μ at the same region and the initial development of peaks in μ at the ends of this region.

4. Discussion

4.1. The Effect of the Initial Conditions and Fault Geometry on the Nucleation Process

The location of the slip event in the earthquake sequence has a large effect on the nucleation process, and especially whether the slip event is the first one, or later in the sequence. Moreover, the effect of roughness is generally larger for the first slip events. The first slip events share similar initial conditions, with initially homogeneous stress along the fault. As b_r increases, segments with preferable orientation slip earlier and under lower average shear load (see Figure 2); thus, the available energy for the rupture process is smaller and the transition between the localization and expansion processes of the rupture is earlier. The earlier transition is accompanied by smaller slip rates (see Figures 3 and 4), which enable more expansion of the rupture before the transition to the dynamic stage. Moreover, the rupture has to propagate through barriers with larger amplitude, which complicates the nucleation process. For $b_r \leq 0.002$, these effects lead to significant increases in l_{nuc} with b_r for the first events. For larger values of b_r, the first events are aseismic or involve mostly aseismic deformation.

For slip events that are later in the sequences, the initial stresses are not constant along the fault and are determined by the rupture process in the previous slip event, which is itself determined by the roughness and finiteness of the fault. The latter has a large effect on the arrest stage of the rupture. The nonconstant initial stresses together with the roughness govern the loading and nucleation stages of the rupture in the later slip events. The small change in l_c with b_r for $b_r \leq 0.002$ for the later events suggests that the effect of the finiteness of the fault on the initial stresses is the most dominant factor in the nucleation process for these values of b_r. This is also reflected in the location where most of these events initiate for $b_r \leq 0.001$ and for some of the slip events on fault with $b_r = 0.002$. For larger values of b_r, the roughness seems to play a larger role.

We consider here only the elastic response of the medium surrounding the fault. For the first slip events in the sequences, the inclusion of more complex rheologies, such as damage, plasticity, or viscoelasticity, is not expected to have a large effect on the nucleation process because the deformations in the medium around the fault are not large yet. At later events there are two competing effects. On the one hand, off-fault inelastic deformation would decrease the stress concentrations at the tips of the fault and, in general, promote more homogeneous initial stresses on the fault, which would lead to a larger effect of roughness during the nucleation stage, as discussed above. On the other hand, the geometric barriers, which introduce substantial complexity into the nucleation process, are expected to be weaker with the inclusion of these rheologies.

We believe that, for the frictional parameters adopted in this study, the fault length considered ($L_f = 40$ m) is sufficient to study the nucleation process and that the main findings of this study are valid also for larger fault lengths. For smooth faults with homogenous initial conditions, l_{nuc} generally decreases with increasing fault length. However, the rate of decrease is quite small for most initial and loading conditions, including those of this study, and declines with increasing fault length (Fang et al., 2010). For rough faults, there is no correlation between the nucleation lengths and whether the rupture initiates next to the center or near the end of the fault; thus, we do not expect different values of l_{nuc} for larger fault lengths.

4.2. Nucleation Length and Fault Stability

In this section, we aim to explain quantitatively the behavior of l_{nuc} in the later slip events, where the nucleation process is generally less complex. Using a two-dimensional static, linear elastic boundary element model, Dieterich and Smith (2009) quantified the additional resistance to slip from fault roughness. They suggested that stresses from geometric irregularities grow linearly with slip and produce backstresses that progressively impede slip. Thus, the relationship between the average slip on the fault, $\overline{D}$, and a uniform stress drop on the fault, $\Delta\tau$, can be approximated by a combined system stiffness as

$$(K_s + K_r)\overline{D} = \Delta\tau, \tag{4}$$

where K_s is the effective stiffness of a slipping patch on a smooth fault, which for an expanding rupture with half length a_{rup} under plane strain condition is given by (Starr, 1928)

$$K_s = \frac{2G^*}{\pi a_{\mathrm{rup}}}, \tag{5}$$

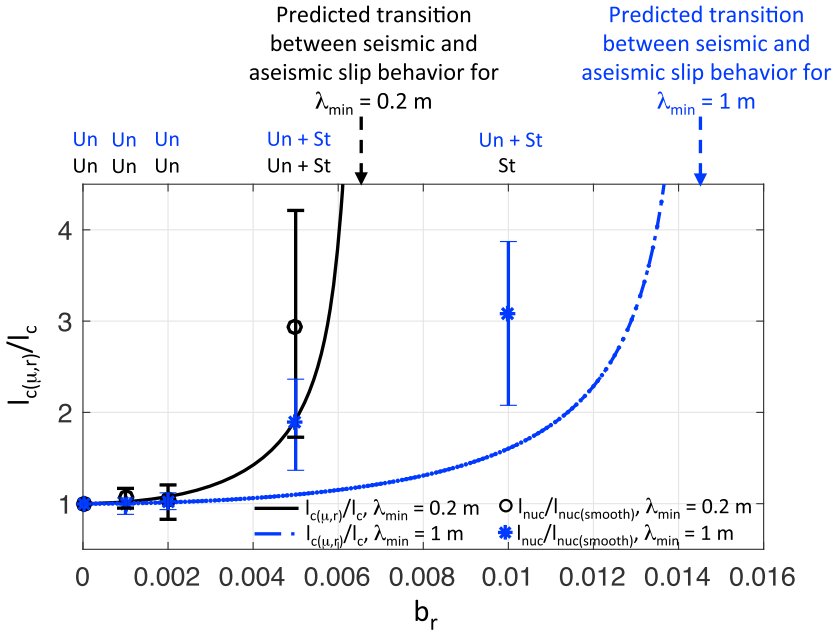

Figure 10. The ratio $l_{c(\mu,r)}/l_c$ as a function of b_r for λ_{min} = 0.2 m (black curve) and 1 m (blue curve). The values of l_{nuc} for the later fast slip events in the simulations normalized by that of the second event on the smooth fault are also shown. The error bars represent the range of the nucleation lengths that were obtained for a given combination of λ_{min} and b_r. The predicted transitions between stable and unstable fault slip behavior are also shown, as well as whether, in the simulations, the faults experienced sequences of only fast slip events (Un), fast and slow slip events (Un + St), and only slow slip events (St).

and K_r is a stiffness accounting for the additional resistance from the roughness. Using slip scaling arguments, Dieterich and Smith (2009) showed that K_r scales with $G^* b_r^2/\lambda_{min}$ and depends weakly on H for $H \geq 0.75$. Fang and Dunham (2013) used a second-order boundary perturbation analysis of small, quasi-static, frictionless, and uniform sliding across a band-limited self-similar interface (H = 1) in an elastic solid to derive a precise expression for the additional shear resistance, or roughness drag, as

$$\tau_{drag} = K_r \overline{D} = \frac{8\pi^3 G^* b_r^2}{\lambda_{min}} \overline{D}. \tag{6}$$

We assume a symmetric expansion process during the nucleation and use a fracture energy balance (e.g., Rubin & Ampuero, 2005), which is a more suitable approach for large a/b values, together with the combined stiffness system described by equations (4)–(6) to derive an approximate expression for the nucleation length on rough faults governed by rate and state friction (Appendix B) as

$$l_{c(\mu,r)} = \frac{2 l_c}{(1 - l_{\mu r}) + \sqrt{(1 - l_{\mu r})}}, \tag{7}$$

with

$$l_{\mu r} = 4\pi^4 \frac{l_c b_r^2}{\lambda_{min}} < 1. \tag{8}$$

Note that $l_{c(\mu,r)}$ reduces to l_c for a smooth fault ($b_r \to 0$). In addition, it becomes infinitely large for $l_{\mu r} \to 1$ and is undefined for $l_{\mu r} > 1$; thus, an earthquake with large slip rates can nucleate only for $l_{\mu r} < 1$. This suggests that the condition in equation (8) provides the frictional and roughness conditions under which faults can slip seismically.

The approximate solution for $l_{c(\mu,r)}$ agrees well with the main trends observed in the simulations for the later events and can be used to estimate the lower bound of l_{nuc} for faults with large b_r. Figure 10 shows the ratio $l_{c(\mu,r)}/l_c$ as a function of b_r for λ_{min} = 0.2 and 1 m, as well as the values of l_{nuc} obtained in the simulations for the later fast slip events, normalized by that of the smooth fault. Similarly to l_{nuc} of the

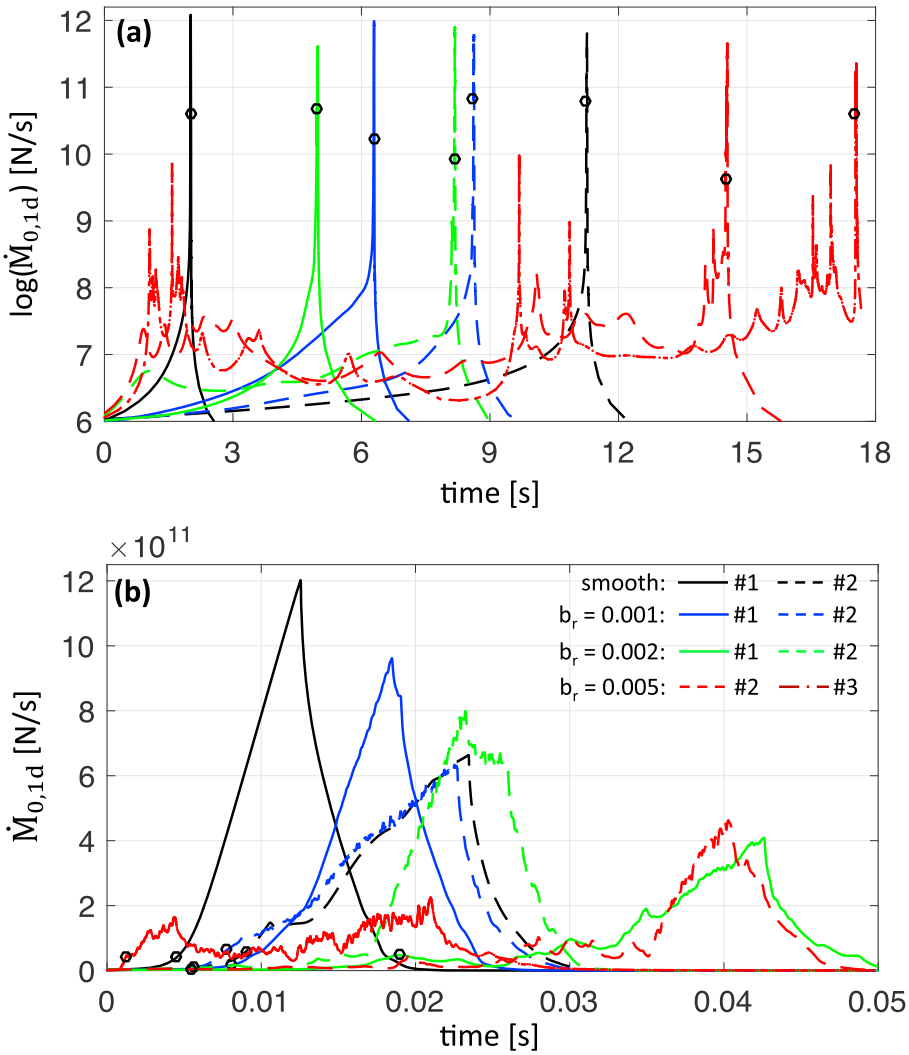

Figure 11. (a) Curves of the evolution of $\dot{M}_{0,1d}$ during 18 s near their maximum values for the first (solid) and later (dashed) slip events in the earthquake sequences shown in Figures 3 and 4, except for the first slip event for $b_r = 0.005$. To show all slip events in a single plot, the curves begin at the time when the moment rate exceeds a value of $\dot{M}_{0,1d} = 10^6$ N/s for the last time before it approaches its maximum value. The black circles denote the transition between the nucleation and the dynamic stages, as defined in this study. (b) The evolution of $\dot{M}_{0,1d}$ during 0.05 s near its maximum value for the same slip events. The curves are aligned such that they all begin when $\dot{M}_{0,1d}$ exceeds a value of 2×10^9 N/s for the last time before it approaches the maximum value. The black circles denote the transition between the nucleation and the dynamic stages.

later events, the change in $l_{c(\mu,r)}$ is very small for $b_r \leq 0.002$. For $\lambda_{min} = 0.2$ m, the ratio $l_{c(\mu,r)}/l_c$ increases rapidly at larger values of b_r and is within the range of the simulation values for $b_r = 0.005$, although at the lower part. For $\lambda_{min} = 1$ m, the ratio increases less rapidly and is below the corresponding simulation values at $b_r = 0.005$ and 0.01. The estimated transitions between seismic and aseismic behavior ($l_{\mu r} = 1$) are consistent with simulations. For $\lambda_{min} = 0.2$, the transition is at $b_r = 0.0065$, and the simulations show that faults with $b_r = 0.005$ experience two or three fast slip events, but faults with $b_r = 0.01$ experience only slow slip events. For $\lambda_{min} = 1$, the transition is at $b_r = 0.0145$, and the simulation shows that faults with $b_r = 0.01$ experience two or three fast slip events.

4.3. Detection of the Nucleation Stage and Its Relationship to the Final Size of the Event

Near-source observations suggest that the seismic nucleation phase can be detected and that it is characterized by a relatively small moment rate with irregular fluctuations, which are followed by quadratic growth in the moment rate as rupture begins to propagate (Ellsworth & Beroza, 1995, 1998). Lapusta and Rice (2003)

performed simulations of earthquake sequences in a 2-D antiplane framework and showed that large earthquakes may have irregular moment rate in the beginning of the dynamic stage because of the heterogeneous stress field caused by arrest of previous events.

The complexities in the nucleation process in the case of rough faults, such as irregular evolution of the slip rates and the rate of expansion of the rupture, also result in fluctuations in the moment rate. Figure 11a shows the evolution of the moment rate per unit length, $\dot{M}_{0,1d}$, in the slip events shown in Figures 3 and 4, except for the first slip event for $b_r = 0.005$. To show all slip events in a single plot, the curves are aligned such that they all begin when $\dot{M}_{0,1d}$ exceeds the value of 10^6 N/s for the last time before it approaches the maximum value. At this scale, $\dot{M}_{0,1d}$ shows irregular behavior mostly for $b_r = 0.005$, with large variations that may be considered as subevents. To examine the behavior near the transition to the dynamic stage, in Figure 11b, the curves are aligned such that they all begin when $\dot{M}_{0,1d}$ exceeds a value of 2×10^9 N/s for the last time before it approaches the maximum value. In the first slip events on a smooth fault and a fault with $b_r = 0.001$, $\dot{M}_{0,1d}$ increases monotonically up to the peak value, while in other events it exhibits irregular fluctuations. The number of the fluctuations and their magnitudes generally increase with increasing b_r. In the two events on the fault with $b_r = 0.002$ and the second event on fault with $b_r = 0.005$, there is a relatively long stage of small and irregular $\dot{M}_{0,1d}$, which is followed by a stage of rapid increase toward the peak value. Note that the transition between these two stages occurs after the beginning of the dynamic stage of the rupture defined in this study.

The behavior of $\dot{M}_{0,1d}$ at the two stages somewhat resembles the seismic nucleation phase observed by Umeda (1990) and Ellsworth and Beroza (1995, 1998). While they observe that the duration, source dimension, and average slip associated with the nucleation phase scale with the moment of the eventual earthquake, we generally observe that the final size of the slip event decreases as $\dot{M}_{0,1d}$ shows a longer stage of irregular behavior. However, we study the behavior of small faults with the largest slip event equivalent to a magnitude 1.5 earthquake, while they examine moderate to large earthquakes, in which the nucleation phases themselves are much larger than the slip events in our study. Nakatani et al. (2000) analyzed the velocity waveforms of 17 microearthquakes ($0.3 \leq M \leq 2.1$) in Japan and showed that microearthquakes that start with a stronger initial rupture tend to grow larger, which is consistent with the trends obtained in our study. It is important to note, however, that other studies do not show a consistent relationship between the beginning of the nucleation phase and the final size of the earthquakes (e.g., Mori & Kanamori, 1996).

The irregular behavior of $\dot{M}_{0,1d}$ for $b_r \geq 0.002$, as well as the increase in l_{nuc} with b_r at these b_r values, increases the potential for detection of the nucleation phase, at least near the beginning of the dynamic stage, when the rupture is larger and the fluctuations are associated with larger deformations on the fault than at earlier stages. However, the lab-scale value of $L = 20$ μm for the characteristic slip distance used in our study leads to small nucleation zones, which are difficult to detect, even for the roughest faults. If the values of L for natural faults are much larger than the values obtained in laboratory experiments (e.g., Marone & Kilgore, 1993; Scholz, 1988) and the roughness parameters that are significant in the rupture process allow seismic behavior, the deformation during the nucleation should be large enough to be detected. However, it is important to note that we consider here only the "aging" formulation for the state evolution law. The slip state evolution law predicts a smaller nucleation length than does the aging law for the values of a and b adopted here (e.g., Ampuero & Rubin, 2008).

5. Conclusions

We study numerically the effects of roughness on the nucleation of earthquakes on faults governed by rate and state friction and subjected to slow loading. Our numerical approach accounts for all stages in the seismic cycle, and in each simulation we model a sequence of two earthquakes or more. This enables studying the effects of heterogeneities left by the arrest of a slip event on the nucleation process in a subsequent event.

Roughness introduces local barriers that complicate the nucleation process and result in asymmetric expansion of the rupture, stages where the rupture expands but the slip rates on the fault decrease, and the generation of new slip pulses, which rerupture regions that already slipped.

A significant effect is observed for whether the slip events are first or later in the earthquake sequence, with larger effects of the roughness for the first events, where the initial conditions are homogenous. For the first events, there is a large increase in the nucleation length with b_r for $b_r \leq 0.002$, and a transition to aseismic or mostly aseismic deformation for larger b_r values. Moreover, in the first events the ruptures always initiate where the local geometry of the fault is most favorable for slip. For slip events later in the sequence, the initial stress field and frictional conditions are determined by the rupture growth and arrest in previous slip events, which are themselves determined by the finiteness of the fault and the roughness. This leads to a trade-off between the effects of the finiteness of the fault and the roughness. For $b_r \leq 0.002$, the effects of finiteness of the fault on the initial stresses are a more dominant factor in the nucleation process, the nucleation length barely changes with b_r, and most of the events initiate close to the ends of the fault. For larger values of b_r, the roughness seems to play a larger role, the nucleation length increases with b_r, and location where the events initiate is more variable.

To explain the behavior of the later events more quantitatively, we derive an approximate solution for the nucleation length on rough faults as $\frac{2l_c}{(1-l_{\mu r})+\sqrt{(1-l_{\mu r})}}$, with $l_{\mu r} = 4\pi^4 \frac{l_c b_r{}^2}{\lambda_{\min}} < 1$. The solution agrees well with the main trends observed in the simulations for the variation of l_{nuc} with b_r and $\lambda_{\min}$ and provides insight on the effect of frictional and roughness properties on the transition between seismic and aseismic slip behavior.

The complexities in the nucleation process are reflected as irregular fluctuations in the moment rate, especially for $b_r \geq 0.002$. The irregular behavior of $\dot{M}_{0,1d}$ and the increase in the nucleation length at these b_r values increase the potential for detection of the later stages in the nucleation process.

Appendix A: Variable Time Step Size

We adopt the following criteria to estimate the time step size at the next time step. (1) Based on the current values of slip rates, we aim that the average incremental slip of the 40 fastest nodes along the fault, Δu_{40}, will be smaller than 0.4 L; (2) To model the healing stage accurately, the size of the next time step cannot be larger than that of the current one by more than 1.5; and (3) at the end of the dynamic stages the time step cannot exceed a value of 50 μs until the kinetic energy in the medium is dissipated. Figure A1 shows the evolutions of $\Delta u_{40,}$ the maximum incremental slip for each time step, Δu_1, and the time step size, Δt, during a simulation on fault with Geo-1, b_r = 0.001, and $\lambda_{\min}$ = 1 m. By adjusting the time step based on the 40 fastest nodes, we significantly reduce the number of time steps during the dynamic stages of the events, which include about 93% of the total number of time steps, but represent the evolution of the friction coefficient well. During the loading and nucleation stages, the slip rate peaks are generally wide and the difference between Δu_1 and Δu_{40} is smaller than 25%; thus, Δu_1 is generally less than 0.5 L. Δu_1 is smaller than 0.3 L during the loading stage (except for six time steps with larger values with maximum of 0.55 L) and increases from 0.3 L to 0.5 L during nucleation stage. During the dynamic stages of the rupture, Δu_1 increases up to values of about 0.9 L. However, considering the evolution of the shear traction and slip rate with slip for a given node (Figure A2), the maximum slip rate, and consequently the maximum incremental slip, is at the stage where the shear stress decreases linearly with slip; thus, the evolution of the friction coefficient is represented well also with slip intervals larger than 0.5 L. Moreover, the observed slip-weakening behavior matches that expected for dynamic ruptures on faults obeying rate and state friction law (e.g., Bizzarri & Cocco, 2003; Rubin & Ampuero, 2005). The observed equivalent slip-weakening distance, $d_c \approx 28L$, agrees with estimate of $d_c = L \ln (v/v_i)$, where v_i is the slip rate prior to the arrival of the rupture tip and is about 10^{-11} m/s for that node. Similarly, the peak to residual shear traction drop, $\tau^{p-r} \approx 32$ MPa, agrees with the estimate of $\tau^{p-r} = b\sigma L \ln (v/v_i)$.

Appendix B: A Fracture Energy Balance-Based Derivation for the Nucleation Length on Rough Faults

Assuming that the ratio a/b is large and promotes expansion and that expansion is relatively symmetric with a uniform stress drop, we use a fracture energy balance approach (e.g., Rubin & Ampuero, 2005) to derive an

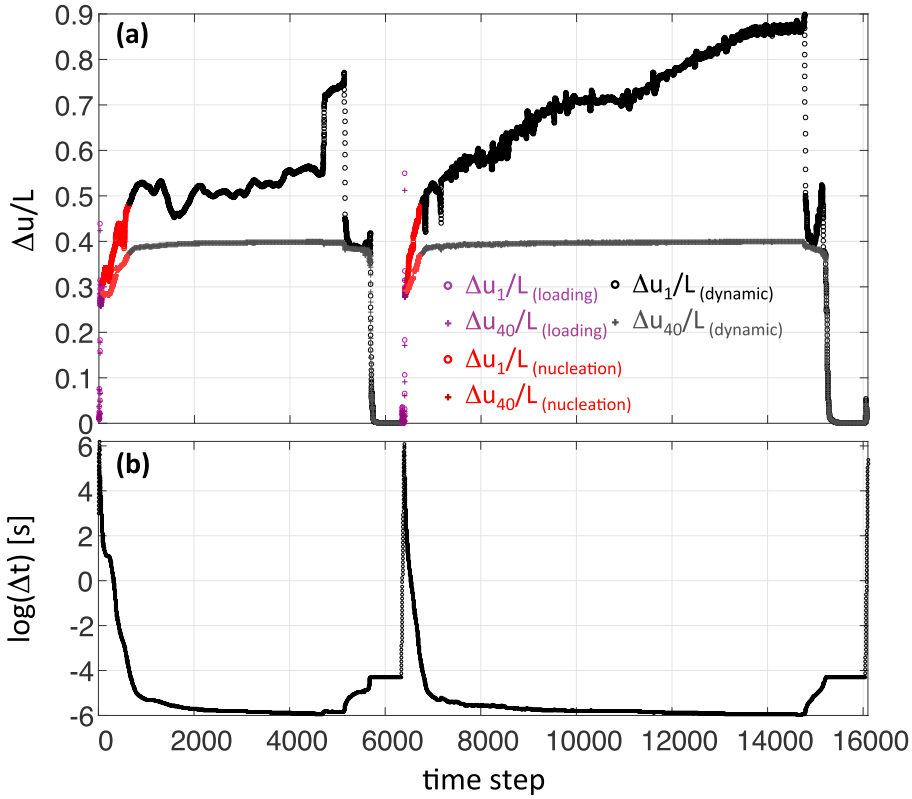

Figure A1. (a) The evolutions of $\Delta u_{40}/L$ (plus symbol) and $\Delta u_1/L$ (circles) during a simulation on a fault with Geo-1, $b_r = 0.001$, and $\lambda_{min} = 1$ m. The simulation includes two events; for each event the loading, nucleation, and dynamic stages are shown in different colors. (b) The evolution of the time step size.

approximate estimation for the nucleation length on rough faults governed by rate and state friction. Consider a growing shear rupture with total length of $2a_{rup}$, the strain energy release per unit length is (Lawn, 1993)

$$\Delta W_0 = \frac{\Delta\tau \overline{D} 2a_{rup}}{2}. \tag{B1}$$

Substituting $\overline{D}$ from equations (4)–(6),

$$\Delta W_0 = \frac{\Delta\tau^2}{2G^*} \frac{a_{rup}}{\frac{1}{\pi a_{rup}} + \frac{4\pi^3 b_r^2}{\lambda_{min}}}. \tag{B2}$$

The reduction in mechanical energy per increment of crack length is given by (Lawn, 1993)

$$G_{energy} = \frac{1}{2}\frac{\partial \Delta W_0}{\partial a_{rup}} = \frac{\Delta\tau^2}{2G^*} \frac{\frac{1}{\pi a_{rup}} + \frac{2\pi^3 b_r^2}{\lambda_{min}}}{\left[\frac{1}{\pi a_{rup}} + \frac{4\pi^3 b_r^2}{\lambda_{min}}\right]^2}. \tag{B3}$$

At the transition from the nucleation to the dynamic stage, the rupture is in equilibrium and G_{energy} is balanced by the fracture energy G_c, which for rate and state friction with large v yields (Rubin & Ampuero, 2005)

$$G_c = \frac{\sigma b L}{2}\left[\ln\left(\frac{v}{v_i}\right)\right]^2, \tag{B4}$$

where v_i denotes the value of v just prior to the arrival of the rupture tip. We note that the derivation does not account for the effect of normal

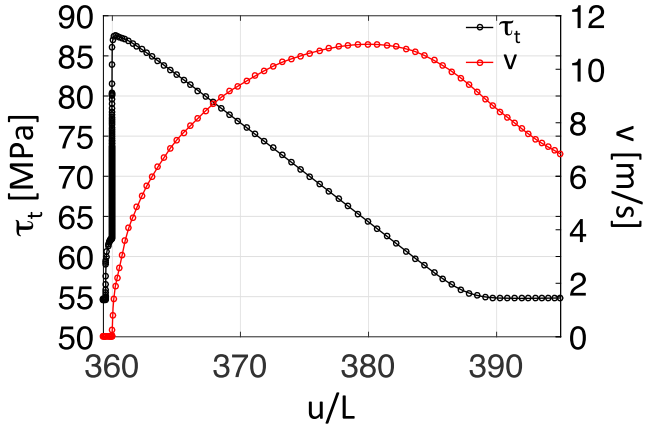

Figure A2. The evolutions of τ_t and v with u/L for a node located at a distance of 10 m from the right end of the fault during the second slip event in a simulation on fault with Geo-1, $b_r = 0.001$, and $\lambda_{min} = 1$ m. Note that the slip is calculated from the beginning of the simulation and that the later stages of the event are not shown.

stress perturbations on G_c, which can induce short slip accelerations transients and even foreshocks during the nucleation process, as observed in the simulations (see Figure 11).

Equating equations (B3) and (B4), substituting the large v estimate of stress drop $\Delta\tau = \sigma(b-a)\ln\left(\frac{v}{v_i}\right)$, and replacing a_{rup} by the half length of the rupture at equilibrium, a_{crit}, give

$$\frac{\frac{1}{\pi a_{\mathrm{crit}}} + \frac{2\pi^3 {b_r}^2}{\lambda_{\min}}}{\left[\frac{1}{\pi a_{\mathrm{crit}}} + \frac{4\pi^3 {b_r}^2}{\lambda_{\min}}\right]^2} = \left(\frac{b}{b-a}\right)^2 \frac{G^* L}{b\sigma}. \tag{B5}$$

We substitute

$$\left(\frac{b}{b-a}\right)^2 \frac{G^* L}{b\sigma} = \frac{\pi}{2} l_c = A \text{ and } \frac{2\pi^3 {b_r}^2}{\lambda_{\min}} = B \tag{B6}$$

and arrange the terms to obtain a quadratic equation as

$$\pi^2 B(4AB-1){a_{\mathrm{crit}}}^2 + \pi(4AB-1)a_{\mathrm{crit}} + A = 0. \tag{B7}$$

The roots of the equation are given by

$$a_{\mathrm{crit}(1,\ 2)} = \frac{(1-4AB) \pm \sqrt{(1-4AB)}}{2\pi B(4AB-1)}, \tag{B8}$$

with a positive value only for

$$a_{\mathrm{crit}} = \frac{(1-4AB) - \sqrt{(1-4AB)}}{2\pi B(4AB-1)}, \quad 1-4AB > 0. \tag{B9}$$

To simplify further, we multiply by $\frac{(1-4AB)+\sqrt{(1-4AB)}}{(1-4AB)+\sqrt{(1-4AB)}}$ and obtain

$$a_{\mathrm{crit}} = \frac{2A}{\pi} \frac{1}{(1-4AB) + \sqrt{(1-4AB)}}, \quad 1-4AB > 0. \tag{B10}$$

The final expression for the nucleation length is given by

$$l_{c(\mu,r)} = 2a_{\mathrm{crit}} = \frac{2l_c}{(1-l_{\mu r}) + \sqrt{(1-l_{\mu r})}}, \quad l_{\mu r} < 1, \tag{B11}$$

where $l_{\mu r} \equiv 4AB = \frac{l_c}{2}\frac{8\pi^4 {b_r}^2}{\lambda_{\min}}$.

Acknowledgments
We thank Allan Rubin, Eric Dunham, and Yoshihiro Kaneko for their thorough reviews and constructive comments. This work was supported by Aramco grant 6500009957 and the Southern California Earthquake Center (SCEC) grant 16108. SCEC is funded by NSF Cooperative Agreement EAR-1033462 and USGS Cooperative Agreement G12 AC20038. Computer code used in this work has been cited in the references, and numerical data are available to anyone upon request.

References

Ampuero, J. P., & Rubin, A. M. (2008). Earthquake nucleation on rate and state faults—Aging and slip laws. *Journal of Geophysical Research*, *113*, B01302. https://doi.org/10.1029/2007JB005082

Bernardi, C., Maday, Y., & Patera, A. T. (1993). *Domain decomposition by the mortar element method, Asymptot. Numer. Methods Partial Differ. Equations with Crit. Parameters*, *NATO ASI Series* (Vol. 384, pp. 269–286). Netherlands: Springer. https://doi.org/10.1007/978-94-011-1810-1_17

Bhattacharya, P., Rubin, A. M., Bayart, E., Savage, H. M., & Marone, C. (2015). Critical evaluation of state evolution laws in rate and state friction: Fitting large velocity steps in simulated fault gouge with time-, slip-, and stress-dependent constitutive laws. *Journal of Geophysical Research: Solid Earth*, *120*, 6365–6385. https://doi.org/10.1002/2015JB012437

Bhattacharya, P., Rubin, A. M., & Beeler, N. M. (2017). Does fault strengthening in laboratory rock friction experiments really depend primarily upon time and not slip? *Journal of Geophysical Research: Solid Earth*, *122*, 6389–6430. https://doi.org/10.1002/2017JB013936

Bistacchi, A., Ashley Griffith, W., Smith, S. A. F., di Toro, G., Jones, R., & Nielsen, S. (2011). Fault roughness at seismogenic depths from LIDAR and photogrammetric analysis. *Pure and Applied Geophysics*, *168*(12), 2345–2363. https://doi.org/10.1007/s00024-011-0301-7

Bizzarri, A., & Cocco, M. (2003). Slip-weakening behavior during the propagation of dynamic ruptures obeying rate- and state-dependent friction laws. *Journal of Geophysical Research*, *108*(B8), 2373. https://doi.org/10.1029/2002JB002198

Brodsky, E. E., Gilchrist, J. J., Sagy, A., & Collettini, C. (2011). Faults smooth gradually as a function of slip. *Earth and Planetary Science Letters*, *302*(1-2), 185–193. https://doi.org/10.1016/j.epsl.2010.12.010

Brown, S. R., & Scholz, C. H. (1985). Broad bandwidth study of the topography of natural rock surfaces. *Journal of Geophysical Research*, *90*, 12,575–12,582. https://doi.org/10.1029/JB090iB14p12575

Bruhat, L., Fang, Z., & Dunham, E. M. (2016). Rupture complexity and the supershear transition on rough faults. *Journal of Geophysical Research: Solid Earth*, *121*, 210–224. https://doi.org/10.1002/2015JB012512

Brunssen, S., Schmid, F., Schafer, M., & Wohlmuth, B. I. (2007). A fast and robust iterative solver for nonlinear contact problems using a primal-dual active set strategy and algebraic multigrid. *International Journal for Numerical Methods in Engineering*, *69*(3), 524–543. https://doi.org/10.1002/nme

Candela, T., Renard, F., Bouchon, M., Brouste, A., Marsan, D., Schmittbuhl, J., & Voisin, C. (2009). Characterization of fault roughness at various scales: Implications of three-dimensional high resolution topography measurements. *Pure and Applied Geophysics*, *166*(10-11), 1817–1851. https://doi.org/10.1007/s00024-009-0521-2

Candela, T., Renard, F., Klinger, Y., Mair, K., Schmittbuhl, J., & Brodsky, E. E. (2012). Roughness of fault surfaces over nine decades of length scales. *Journal of Geophysical Research*, *117*, B08409. https://doi.org/10.1029/2011JB009041

Dieterich, J. H. (1978). Preseismic fault slip and earthquake prediction. *Journal of Geophysical Research*, *83*, 3940–3948. https://doi.org/10.1029/JB083iB08p03940

Dieterich, J. H. (1979). Modeling of rock friction: 1. Experimental results and constituve equations. *Journal of Geophysical Research*, *116*, 790–806. https://doi.org/10.1007/BF00876539

Dieterich, J. H. (1992). Earthquake nucleation on faults with rate-and state-dependent strength. *Tectonophysics*, *211*(1-4), 115–134. https://doi.org/10.1016/0040-1951(92)90055-B

Dieterich, J. H., & Smith, D. E. (2009). Nonplanar faults: Mechanics of slip and off-fault damage. *Pure and Applied Geophysics*, *166*(10-11), 1799–1815. https://doi.org/10.1007/s00024-009-0517-y

Dunham, E. M., Belanger, D., Cong, L., & Kozdon, J. E. (2011). Earthquake ruptures with strongly rate-weakening friction and off-fault plasticity, Part 2: Nonplanar faults. *Bulletin of the Seismological Society of America*, *101*(5), 2308–2322. https://doi.org/10.1785/0120100076

Ellsworth, W. L., & Beroza, G. C. (1995). Seismic evidence for an earthquake nucleation phase. *Science*, *268*(5212), 851–855. https://doi.org/10.1126/science.268.5212.851

Ellsworth, W. L., & Beroza, G. C. (1998). Observation of the seismic nucleation phase in the Ridgecrest, California, earthquake sequence. *Geophysical Research Letters*, *25*, 401–404. https://doi.org/10.1029/97GL53700

Fang, Z., Dieterich, J. H., & Xu, G. (2010). Effect of initial conditions and loading path on earthquake nucleation. *Journal of Geophysical Research*, *115*, B06313. https://doi.org/10.1029/2009JB006558

Fang, Z., & Dunham, E. M. (2013). Additional shear resistance from fault roughness and stress levels on geometrically complex faults. *Journal of Geophysical Research: Solid Earth*, *118*, 3642–3654. https://doi.org/10.1002/jgrb.50262

Gitterle, M., Popp, A., Gee, M. W., & Wall, W. A. (2010). Finite deformation frictional mortar contact using a semi-smooth Newton method with consistent linearization. *International Journal for Numerical Methods in Engineering*, *84*, 543–571. https://doi.org/10.1002/nme.2907

Hüeber, S., Stadler, G., & Wohlmuth, B. I. (2008). A primal–dual active set algorithm for three-dimensional contact problems with Coulomb friction. *SIAM Journal on Scientific Computing*, *30*(2), 572–596. https://doi.org/10.1137/060671061

Hüeber, S., & Wohlmuth, B. I. (2005). A primal-dual active set strategy for non-linear multibody contact problems. *Computer Methods in Applied Mechanics and Engineering*, *194*(27-29), 3147–3166. https://doi.org/10.1016/j.cma.2004.08.006

Kaneko, Y., & Ampuero, J. P. (2011). A mechanism for preseismic steady rupture fronts observed in laboratory experiments. *Geophysical Research Letters*, *38*, L21307. https://doi.org/10.1029/2011GL049953

Kaneko, Y., & Lapusta, N. (2008). Variability of earthquake nucleation in continuum models of rate-and-state faults and implications for aftershock rates. *Journal of Geophysical Research*, *113*, B12312. https://doi.org/10.1029/2007JB005154

Kaneko, Y., Nielsen, S. B., & Carpenter, B. M. (2016). The onset of laboratory earthquakes explained by nucleating rupture on a rate-and-state fault. *Journal of Geophysical Research: Solid Earth*, *121*, 6071–6091. https://doi.org/10.1002/2016JB013143

Kato, N., & Hirasawa, T. (1996). Effects of strain rate and strength nonuniformity on the slip nucleation process: A numerical experiment. *Tectonophysics*, *265*(3-4), 299–311. https://doi.org/10.1016/S0040-1951(96)00089-3

Klinger, Y. (2010). Relation between continental strike-slip earthquake segmentation and thickness of the crust. *Journal of Geophysical Research*, *115*, B07306. https://doi.org/10.1029/2009JB006550

Lapusta, N., & Rice, J. R. (2003). Nucleation and early seismic propagation of small and large events in a crustal earthquake model. *Journal of Geophysical Research*, *108*(B4), 2205. https://doi.org/10.1029/2001JB000793

Latour, S., Schubnel, A., Nielsen, S., Madariaga, R., & Vinciguerra, S. (2013). Characterization of nucleation during laboratory earthquakes. *Geophysical Research Letters*, *40*, 5064–5069. https://doi.org/10.1002/grl.50974

Lawn, B. (1993). *Fracture of brittle solids* (2nd ed.). New York: Cambridge University Press. https://doi.org/10.1017/CBO9780511623127

Marone, C. (1998). Laboratory-derived friction laws and their application to seismic faulting. *Annual Review of Earth and Planetary Sciences*, *26*(1), 643–696. https://doi.org/10.1146/annurev.earth.26.1.643

Marone, C., & Kilgore, B. (1993). Scaling of the critical slip distance for seismic faulting with shear strain in fault zones. *Nature*, *362*(6421), 618–621. https://doi.org/10.1038/362618a0

McLaskey, G. C., & Kilgore, B. D. (2013). Foreshocks during the nucleation of stick-slip instability. *Journal of Geophysical Research: Solid Earth*, *118*, 2982–2997. https://doi.org/10.1002/jgrb.50232

Mori, J., & Kanamori, H. (1996). Initial rupture of earthquakes in the 1995 Ridgecrest, California sequence. *Geophysical Research Letters*, *23*, 2437–2440. https://doi.org/10.1029/96GL02491

Nakatani, M., Kaneshima, S., & Fukao, Y. (2000). Size-dependent microearthquake initiation inferred from high-gain and low-noise observations at Nikko district, Japan. *Journal of Geophysical Research*, *105*, 28,095–28,109.

Newmark, N. M. (1959). A method of computation for structural dynamics. *Journal of the Engineering Mechanics Division*, *85*(3), 67–94.

Nielsen, S., Taddeucci, J., & Vinciguerra, S. (2010). Experimental observation of stick-slip instability fronts. *Geophysical Journal International*, *180*(2), 697–702. https://doi.org/10.1111/j.1365-246X.2009.04444.x

Noda, H., Lapusta, N., & Kanamori, H. (2013). Heterogeneous stress change and implications for earthquake physics. *Geophysical Journal International*, *193*, 1691–1712. https://doi.org/10.1093/gji/ggt074

Ohnaka, M. (2003). A constitutive scaling law and a unified comprehension for frictional slip failure, shear fracture of intact rock, and earthquake rupture. *Journal of Geophysical Research*, *108*(B2), 2080. https://doi.org/10.1029/2000JB000123

Ohnaka, M., & Shen, L. (1999). Scaling of the shear rupture process from nucleation to dynamic propagation: Implications of geometric irregularity of the rupturing surfaces. *Journal of Geophysical Research*, *104*, 817–844. https://doi.org/10.1029/1998JB900007

Okubo, P. G., & Dieterich, J. H. (1984). Effects of physical fault properties on frictional instabilities produced on simulated faults. *Journal of Geophysical Research*, *89*, 5817–5827. https://doi.org/10.1029/JB089iB07p05817

Popp, A., Gee, M. W., & Wall, W. A. (2009). A finite deformation mortar contact formulation using a primal–dual active set strategy. *International Journal for Numerical Methods in Engineering*, *79*(11), 1354–1391. https://doi.org/10.1002/nme.2614

Power, W. L., & Tullis, T. E. (1991). Euclidean and fractal models for the description of rock surface roughness. *Journal of Geophysical Research*, *96*, 415–424. https://doi.org/10.1029/90JB02107

Power, W. L., Tullis, T. E., Brown, S. R., Boitnott, G. N., & Scholz, C. H. (1987). Roughness of natural fault surfaces. *Geophysical Research Letters*, *14*, 29–32. https://doi.org/10.1029/GL014i001p00029

Rathbun, A. P., & Marone, C. (2013). Symmetry and the critical slip distance in rate and state friction laws. *Journal of Geophysical Research: Solid Earth*, *118*, 3728–3741. https://doi.org/10.1002/jgrb.50224

Renard, F., Voisin, C., Marsan, D., & Schmittbuhl, J. (2006). High resolution 3D laser scanner measurements of a strike-slip fault quantify its morphological anisotropy at all scales. *Geophysical Research Letters*, *33*, L04305. https://doi.org/10.1029/2005GL025038

Rubin, A. M., & Ampuero, J. P. (2005). Earthquake nucleation on (aging) rate and state faults. *Journal of Geophysical Research*, *110*, B11312. https://doi.org/10.1029/2005JB003686

Ruina, A. (1983). Slip instability and state variable friction law. *Journal of Geophysical Research*, *88*, 10,359–10,370. https://doi.org/10.1029/JB088iB12p10359

Sagy, A., Brodsky, E. E., & Axen, G. J. (2007). Evolution of fault-surface roughness with slip. *Geology*, *35*(3), 283–286. https://doi.org/10.1130/G23235A.1

Scholz, C. H. (1988). The critical slip distance for seismic faulting. *Nature*, *336*(6201), 761–763. https://doi.org/10.1038/336761a0

Scholz, C. H. (Ed.) (2002). *The mechanics of earthquakes and faulting* (2nd ed.). Cambridge, UK: Cambridge University Press. https://doi.org/10.1017/CBO9780511818516

Shi, Z., & Day, S. M. (2013). Rupture dynamics and ground motion from 3-D rough-fault simulations. *Journal of Geophysical Research: Solid Earth*, *118*, 1122–1141. https://doi.org/10.1002/jgrb.50094

Starr, A. T. (1928). Slip in a crystal and rupture in a solid due to shear. *Mathematical Proceedings of the Cambridge Philosophical Society*, *24*(04), 489–500. https://doi.org/10.1017/S0305004100014626

Tal, Y. (2017). *The role of roughness in earthquake source physics*. Cambridge, MA: Massachusetts Institute of Technology.

Tal, Y., & Hager, B. H. (2017). Dynamic mortar finite element method for modeling of shear rupture on frictional rough surfaces. *Computational Mechanics*. https://doi.org/10.1007/s00466-017-1475-3

Umeda, Y. (1990). High-amplitude seismic waves radiated from the bright spot of an earthquake. *Tectonophysics*, *175*, 81–92.

Wohlmuth, B. I. (2000). A mortar finite element method using dual spaces for the Lagrange multiplier. *SIAM Journal on Numerical Analysis*, *38*(3), 989–1012. https://doi.org/10.1137/S0036142999350929